Chapter 9
Thermal Neutron Holography

B. Sur, R.B. Rogge, V.N.P. Anghel, and J. Katsaras

Abstract X-ray and neutron diffraction techniques have for almost a century produced results that provide important insights into materials of interest to a wide range of scientific and technological disciplines. However, traditional diffraction techniques have their limits, and these limits are best exemplified by the fact that certain important materials (e.g., integral proteins) are difficult if not impossible to crystallize — diffraction techniques usually require high-quality single crystals. Recently developed atomic resolution X-ray and neutron holography techniques offer the promise to resolve the structures of difficult-to-crystallize materials to atomic resolution. This chapter will discuss the latest developments in neutron holography and the challenges that must be overcome to make the technique a viable tool.

Keywords X-ray holography · Neutron holography · Inside source holography · Inside detector holography · Protein crystallography

9.1 Introduction

Holography can be traced to Bragg's [1] X-ray work and Gabor's [2] electron interference microscope. Although the technique lay dormant for a number of decades, there has been increasing interest in its development as implied by the increasing number of publications on atomic-resolution holography using either electrons [3–7] or hard X rays [8–13]. Moreover, the feasibility of atomic-resolution thermal neutron holography, either the "inside source" or "inside detector" type, was experimentally demonstrated [14–16], and a theory was developed showing that the diffraction pattern of plane waves incident on a sample with a uniformly random distribution of incoherent scatterers

J. Katsaras (✉)
National Research Council, Chalk River Laboratories, Chalk River, ON K0J 1J0, Canada
e-mail: john.katsaras@nrc.gc.ca

I.S. Anderson et al. (eds.), *Neutron Imaging and Applications*,
Neutron Scattering Applications and Techniques, DOI 10.1007/978-0-387-78693-3_9,

(e.g., ^{1}H in a polymeric material) per unit cell is the same as that from a sample with a single incoherent scatterer per unit cell [17]. There is interest in the possibility of using neutron holography to reconstruct, to atomic resolution, the three– dimensional (3D) structure of materials rich in hydrogen that are presently difficult to crystallize (e.g., membrane-associated proteins).

Dennis Gabor (1900–1979) developed holography as a technique to improve the resolution of the electron microscope while working for the British Thomson-Houston Company (Rugby, England). A patent was filed in 1947 [18], but the general field did not advance until the invention of the laser [19, 20] (the process of stimulated emission was first theorized by Einstein in 1917) [21]. The first 3D holograms were made by Denisyuk [22] in 1962 (reflection hologram) and later that year by Leith and Upatnieks at the University of Michigan (transmission hologram) [23]. Since then, optical holography has been extensively used in optical devices (e.g., holographic lens for heads-up displays), security (e.g., credit cards), scanners, computer memory storage, medicine, and a variety of other applications. For example, holographic interferometry is a precise technique for measuring changes in the dimensions of an object, and digital cameras with holographic capabilities are able to focus in poor contrast conditions.

For many decades, X-ray diffraction has been relied upon to determine the 3D structure of a number of crystalline materials, the prerequisite being a very high-quality single crystal. However, even when the requisite sample was made available, the technique suffered from the so-called "phase problem" — that is, the phase information was not recorded. As a result, a number of isomorphous crystals had to be grown to allow for the direct solution of molecular structure — at increased cost and time. It should also be pointed out that, in some cases, isomorphous derivatives were impossible to produce. Recently, however, synchrotron sources with their tunable X-ray beams have revolutionized crystallography by allowing the development of multiple-wavelength anomalous dispersion (MAD), a technique used to obtain reliable phase information. Now a single crystal serves the purpose of several different metal-containing crystals and has the added advantage of faster data collection times. Despite these advances, the need for high-quality crystals remains.

Both holography and crystallographic techniques, such as MAD, solve the phase problem in the case of 3D materials. Holographic techniques, however, have the added advantage that only orientational order is required; that is, translational symmetry is not necessary. In addition to imaging crystalline materials, holography is also suitable for imaging noncrystalline materials (e.g., nematic liquid crystals) or poorly crystallized membrane-associated proteins.

Although the idea of atomic-resolution holography has its roots in Bragg's [1] X-ray work and Gabor's [2] electron interference microscope, atomic-resolution holography did not evolve until Szöke [24] pointed out that photo-excited atoms within a sample emit highly coherent outgoing electrons or fluorescent X rays. The interference between the unperturbed wave from the photoexcited atom (reference wave) and waves scattered from neighboring atoms (object waves) thus permitted the realization of atomic-resolution

holography (Fig. 9.1). Of course, evidence for atomic-resolution holography existed as far back as the early twentieth century in the experiments of Kikuchi [25] and Kossel [26].

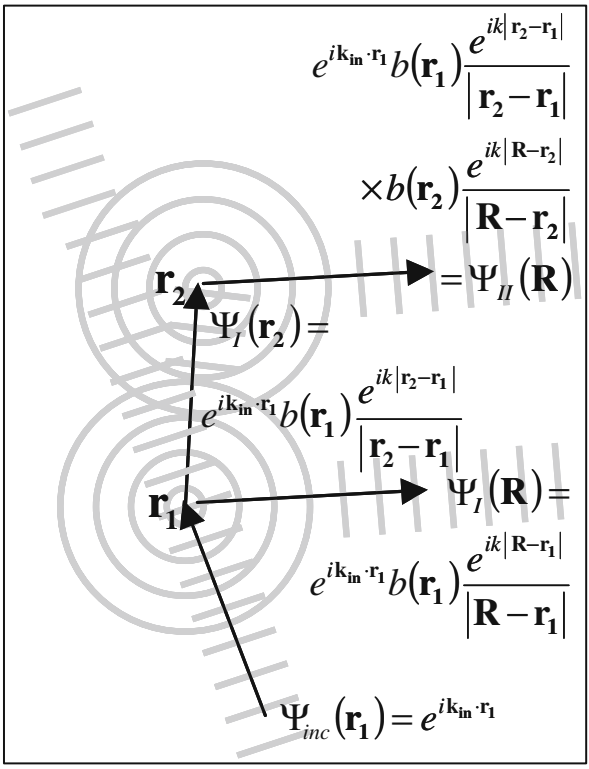

Fig. 9.1 (A) Schematic depiction of second-order plane-wave scattering. The incident neutron plane wave Ψ_{inc} interacts with an atom at $\mathbf{r}_1$, producing a primary spherical wave (S wave) Ψ_I. This primary S wave interacts with a second atom at $\mathbf{r}_2$, producing a secondary S wave Ψ_{II}. The interference between the primary and secondary S waves leads to an intensity modulation (hologram) detected at $\mathbf{R}$. The detected intensity (evaluated for incident and detected wave vectors, $\mathbf{k}_{in}$ and $\mathbf{k}_{out}$) is given as $I = \Psi_I^*\Psi_I + 2\mathrm{Re}\left(\Psi_I^*\Psi_{II}\right) + \Psi_{II}^*\Psi_{II}$. Figure adapted from Sur et al. [17]. See Ref. [17] or Sect. 9.5 of this paper for details

9.2 Atomic-Resolution Holography

There are two kinds of holographic methods capable of atomic resolution: inside source and inside detector. The inside source method [24] uses some of the atoms making up the sample as independent sources of coherent illumination. In the case of X-ray holography and certain types of electron holography (e.g., Auger holography), the radiation generated by atomic de-excitation manifests itself in the form of nearly spherical waves (S waves). This radiation

can either pass through the sample unperturbed (reference wave) or be scattered by the surrounding atoms (object wave). The interference between the reference and object beams produces the hologram.

In the inside detector method developed by Gog et al. [9, 27], the inside source holography beam paths can be reversed and the source and detector exchanged. In other words, an incident plane wave can reach the photoexcitable atom in a crystal unperturbed (reference wave) or after it has scattered off other atoms in the sample (object wave). The interference between these two beams dictates the fluorescence intensity given off by the photoexcitable atom, which is now the detector. When the incident beam is scanned, the phase relation between the reference and object waves leads to oscillations of the fluorescent intensity [28] and forms a hologram.

9.3 Neutrons

In 1932, James Chadwick [29, 30] discovered the neutron — first postulated by Rutherford [31]—a neutral, subatomic elementary particle found in all atomic nuclei except hydrogen nuclei. A neutron's mass is similar to that of a proton, but a neutron possesses a nuclear spin of ½ and a magnetic moment. Neutrons are stable only when bound in an atomic nucleus; an unstable free neutron has a mean lifetime of approximately 900 s and decays into a proton, an electron, and an antineutrino [32].

Even though the neutron's interaction with atomic nuclei is weak, the scattering power (cross section) of an atom is not related to its atomic number. Therefore, neighboring elements in the periodic table can have substantially different scattering cross sections. It is important to note that the interaction of a neutron with the nucleus of an atom allows for an element's isotopes to be differentiated. An example is the isotopic substitution of ^{1}H (hydrogen) for ^{2}H (deuterium), a technique commonly used in the study of polymeric and biologically relevant materials. Hydrogen has a negative coherent scattering length ($b_{coh} = -3.74 \times 10^{-15}$ m), lending it "contrast" when surrounded by other, positive-scattering-length atoms. For biological samples, intrinsically rich in hydrogen, judicious substitution of ^{2}H ($b_{coh} = +6.67 \times 10^{-15}$ m) for ^{1}H provides a powerful method for selectively tuning the "contrast" of a given macromolecule. One can therefore accentuate or nullify the scattering from particular parts of a macromolecular complex by selective deuteration [33]. Of importance to holography is that ^{1}H has a large incoherent cross section for thermal neutrons ($\sigma_i = 80$ barns), producing S waves similar to the de-excitation of a photoexcitable atom in X-ray holography. Unlike forms of electromagnetic radiation that interact primarily with electrons, neutrons interact directly with nuclei and are, to first order, equally capable of imaging light atoms and heavy atoms. Consequently, atomic-resolution holographic images of materials comprising entirely light atoms can be obtained, a great advantage in the study of polymers and biologically relevant materials.

Neutrons suitable for scattering experiments are presently being produced either by nuclear reactors (e.g., the 120-MW National Research Universal [NRU], Chalk River, Ontario) via the fission of uranium nuclei or by spallation sources (Spallation Neutron Source, Oak Ridge, Tennessee), in which accelerated subatomic particles (e.g., protons) strike a target (e.g., tungsten, lead, or liquid mercury), spalling neutrons from the target material's nuclei (for further details, refer to the instrumentation chapter, which is online at http://www.springer.com/series/8141).

9.4 Neutron Holography and *K* Lines

The feasibility of atomic-resolution neutron holography was discussed by Cser et al. [34] on the basis of the large incoherent thermal neutron cross section exhibited by ^{1}H atoms. Experimentally, neutron holography was demonstrated by Sur et al. [14] using a single crystal of natural simpsonite, a rare oxide mineral of aluminum and tantalum first discovered in western Australia [35] in 1939. The mineral, with the chemical formula $Al_4Ta_3O_{13}(OH)$, was examined using X-ray diffraction [36] in the same year as its discovery; more recently, X-ray diffraction has been used to determine the crystal structure in the trigonal space group *P3* with unit cell parameters $a = 7.386(1)$ Å and $c = 4.516(1)$ Å [37]. More important, simpsonite contains only one ^{1}H atom per crystallographic unit cell and was shown to lend itself ideally to holographic reconstruction.

The following year, Sur et al. [15] reported the observation of *K* lines (representing, collectively, Kossel and Kikuchi lines) produced by monochromatic thermal neutrons interacting with a potassium dihydrogen phosphate (KDP) single crystal. *K* lines contain phase information, further establishing the experimental basis for direct crystallographic phasing of atomic structures containing incoherent scatterers via thermal neutron inside source holography.

The interaction of single-frequency plane waves with a periodic potential, formulated in the Born approximation, produces diffraction intensities in discrete directions commonly known as Bragg reflections. Similarly, single-frequency *S* waves interacting with a 3D periodic potential (e.g., an atomic lattice) give rise to sharp conical intensity variations. Viewed on a surface, the conic sections appear as lines.

Nearly spherical single-frequency electromagnetic waves are obtained by electronic de-excitations of atoms (e.g., fluorescence, photoemission) within the crystal sample itself, an "inside source," or a source in close proximity to the sample. In 1922 Clark and Duane [38] predicted the resulting line structures for X rays, which were experimentally observed using a single crystal of copper in 1934 by Kossel, Loeck, and Voges [26]. For X rays, such lines are therefore commonly referred to as Kossel lines. A theoretical explanation was subsequently provided in 1935 by von Laue [39]. Spherical waves can also be generated by dynamical effects (e.g., multiple and inelastic scattering); the resulting

lines were first observed by Kikuchi [25] in electron scattering studies using mica plates of varying thicknesses. Thus such lines are generally referred to as Kikuchi lines. In the present case, thermal neutron S waves are generated by incoherent elastic scattering from hydrogen. The fundamental scattering process that gives rise to the characteristic lines — S wave interaction with the crystal lattice — is the same as for Kossel and Kikuchi lines; therefore, they are collectively referred to as K lines.

The K line intensity pattern depends on the relative position of the periodic scatterers with respect to the S wave source (i.e., the crystallographic phase of the scattering structure function). Thus K lines provide the signal for direct 3D, atomic-resolution imaging techniques (holography) for single crystals via the inside source or inside detector concept.

Atomic nuclei are, to a very good approximation, point or pure S wave scatterers of thermal neutron waves. Hydrogen atoms have a large bound, spin-incoherent cross section, $\sigma_i = 80$ barns, for unpolarized thermal neutrons. An unpolarized, parallel, thermal neutron beam interacting with a single crystal containing hydrogen atoms should therefore give rise to both Bragg reflections, from the incident plane-wave neutron beam, and K lines, from the S waves produced by the incoherent scattering from the ^{1}H atoms.

9.5 Theory

To gain an understanding of the process, consider a single-point S wave source of amplitude a at the origin surrounded by a distribution of weak point or purely S wave scatterers described by a coherent scattering length density $b(\mathbf{r})$. Then, in the Born approximation, the unperturbed or reference wave is

$$\Psi_{(\mathrm{ref})}(\mathbf{r}) = \frac{a\mathrm{e}^{\mathrm{i}|\mathbf{k}||\mathbf{r}|}}{|\mathbf{r}|} \ , \tag{9.1}$$

and the scattered or object wave is

$$\Psi_{\mathrm{obj}}(\mathbf{r}) = a \int_{r_0} \frac{b(\mathbf{r}_0)\mathrm{e}^{\mathrm{i}|\mathbf{k}|(|\mathbf{r}_0|+|\mathbf{r}-\mathbf{r}_0|)}}{|\mathbf{r}_0||\mathbf{r}-\mathbf{r}_0|}\mathrm{d}\,\mathbf{r}_0 \ . \tag{9.2}$$

The total wave amplitude, Ψ_{tot} for a detector at $\mathbf{R}$ is given by $\Psi_{\mathrm{ref}}(\mathbf{R}) + \Psi_{\mathrm{obj}}(\mathbf{R})$. The detected intensity, $I_{1S}(\mathbf{R})$, is then $\Psi^*_{\mathrm{tot}}\,\Psi_{\mathrm{tot}}$. Using the far field diffraction condition (i.e., $R >> r$) and defining the outgoing wave vector in the detector direction as $\mathbf{k}_{out} = k\,\hat{\mathbf{R}}$, the detected intensity is then given as

$$I_{1S} \cong \frac{a^* a}{R^2}[1 + 2\mathrm{Re}[\chi(\mathbf{k}_{\mathrm{out}})] + |\chi(\mathbf{k}_{\mathrm{out}})|^2] \ , \tag{9.3}$$

where the intensity modulation function is

$$\chi(\mathbf{k}_{\text{out}}) = \int_{r_0} \frac{b(\mathbf{r}_0)\mathrm{e}^{\mathrm{i}(kr_0 - \mathbf{k}_{\text{out}}\cdot\mathbf{r}_0)}}{r_0}\mathrm{d}\,\mathbf{r}_0 \ . \tag{9.4}$$

In the case of inside source holography, the scattering length distribution $b(\mathbf{r})$ is reconstructed by a Fourier inversion of the observed modulation intensity [14].

To gain an understanding of K lines, consider this expression [Eq. (9.4)]. In reciprocal space, the modulation function (aside from constants) is given by

$$\chi(\mathbf{k}_{\text{out}}) = \int \frac{B(\mathbf{q})}{|\mathbf{q}|^2 - 2\mathbf{k}_{\text{out}}\cdot\mathbf{q}}\mathrm{d}\mathbf{q} \ , \tag{9.5}$$

where $B(\mathbf{q})$ is the Fourier transform of $b(\mathbf{r})$.

In the case of a crystal lattice, the 3D scattering potential is completely specified by the magnitude and phase of the structure function F_{hkl} at discrete points in reciprocal space. The reciprocal lattice points are given by $\boldsymbol{\tau}_{hkl} = h\mathbf{b}_1 + k\mathbf{b}_2 + l\mathbf{b}_3$, where $\mathbf{b}_1$, $\mathbf{b}_2$, and $\mathbf{b}_3$ are three reciprocal lattice basis vectors. The integral in Eq. (9.5) then becomes a sum over all hkl, namely

$$\chi(\mathbf{k}_{\text{out}}) = \sum_{hkl} \frac{F_{hkl}}{|\tau_{hkl}|^2 - 2\mathbf{k}_{\text{out}}\cdot\tau_{hkl}} \ . \tag{9.6}$$

For every pair of discrete points $\pm\boldsymbol{\tau}_{hkl}$ located within a sphere of radius $2k$, the zeros in the denominator of Eq. (9.6) cause the modulation to go to infinity in $\mathbf{k}_{\text{out}}$ directions whose locus is a cone with axis along $\pm\boldsymbol{\tau}_{hkl}$ and full opening angle 2θ, satisfying the relation $2k\cos\theta = \tau_{hkl}$. Viewed on the surface of a hemisphere of radius k_{out}, the intersections of the cones with the hemisphere are K line rings centered on $\boldsymbol{\tau}_{hkl}$. These K line rings can readily be calculated for any hkl relative to the crystal coordinate system of a known structure. For example, a selection of K lines expected for the structure of KDP in a particular sample orientation is shown in Fig. 9.2A on the surface of a hemisphere $\mathbf{k}_{\text{out}}/|\mathbf{k}_{\text{out}}|$ with $|\mathbf{k}_{\text{out}}| = 4.8$ Å^{-1} [15]. The incident plane wave, $\mathbf{k}_{in}$, will also produce Bragg peaks, which will appear as discrete points on the surface of the hemisphere, when condition $\mathbf{k}_{\text{out}} - \mathbf{k}_{\text{in}} = \boldsymbol{\tau}_{hkl}$ is satisfied (Fig. 9.2A).

In a high-resolution experiment, K lines are readily identified by their characteristic fine structure [27]. However, K line fine structure is affected by factors such as

- sample size and shape;
- dynamics or higher-order partial wave scattering in both the coherent and incoherent scatterers, leading to a broadening of the signal and a nonuniform reference wave intensity; and
- wavelength spread and angular resolution.

All of these effects conspire to mute the sharp modulations characteristic of K lines, but they still produce modulations along the lines (Fig. 9.2B).

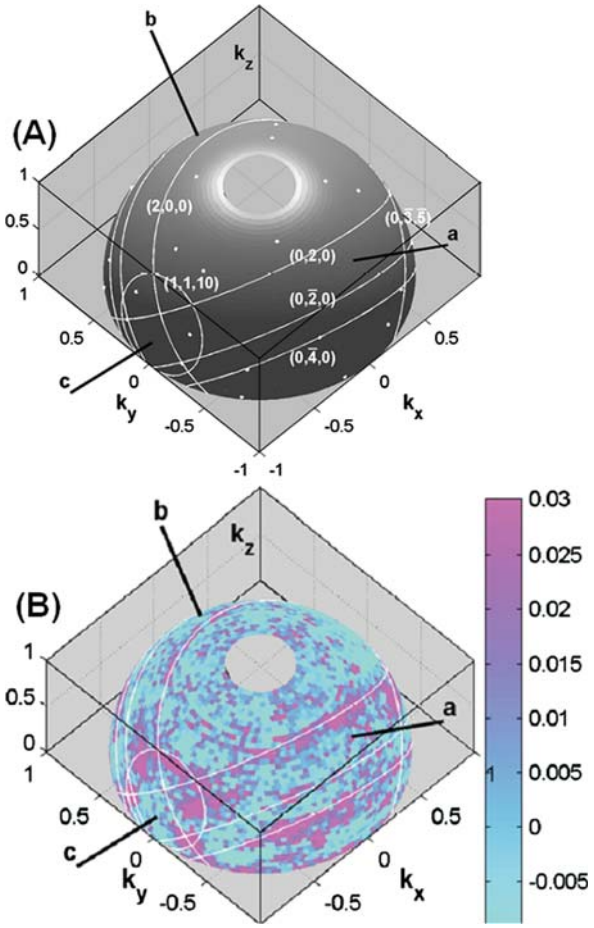

Fig. 9.2 (**A**) Calculated K lines for the various KDP lattice planes for $\lambda = 1.30$ Å neutrons. In addition to the K lines, the locations of Bragg reflections are shown as white spots. The orientation of the crystal with respect to the sphere-of-scattering ($\mathbf{k}_{in} \parallel k_z$) is depicted by the crystallographic axes a, b, and c. (**B**) KDP holographic data corrected for background, Debye-Waller factor, and sample shape. K lines appear as bands of scattering corresponding to the *white lines* in (A). Figure adapted from Sur et al. [15]

9.6 Reconstruction of the Diffraction Patterns from *S* Wave Scatterers

According to Eqs. (9.3) and (9.4), the experimentally observed hologram modulation function $\chi(\mathbf{k})$ produced by the interaction of a weak S wave coherent scattering length distribution $b(\mathbf{r})$ with either a single incoherent point scatterer or with a uniform distribution of incoherent scatterers is given, aside from constants, by

$$\chi(\mathbf{k}) \sim \int_{\text{all space}} \mathrm{Re}\left(\frac{b(\mathbf{r})}{r} e^{[i(kr-\mathbf{k}\cdot\mathbf{r})]}\right) d\mathbf{r} + O\left(b^2\right) . \quad (9.7)$$

The conditions for pure S wave weak scattering are particularly well satisfied for unpolarized thermal neutron scattering from nuclei. Additionally, for most nuclei, the thermal neutron coherent scattering lengths are almost purely real and have the same sign. The real part of the coherent scattering length distribution can be directly reconstructed from the measured hologram modulation function using the following relations.

$$\tilde{b}_{\text{even}}(\mathbf{r}) = \frac{b_{\text{real}}(\mathbf{r}) + b_{\text{real}}(-\mathbf{r})}{kr} \cos(kr) \propto \int_{\text{constant}|\mathbf{k}|} \chi(\mathbf{k}) \cos(\mathbf{k}\cdot\mathbf{r}) d\mathbf{k} . \quad (9.8)$$

$$\tilde{b}_{\text{odd}}(\mathbf{r}) = \frac{b_{\text{real}}(\mathbf{r}) - b_{\text{real}}(-\mathbf{r})}{kr} \sin(kr) \propto \int_{\text{constant}|\mathbf{k}|} \chi(\mathbf{k}) \sin(\mathbf{k}\cdot\mathbf{r}) d\mathbf{k} . \quad (9.9)$$

Strictly speaking, for a single wavelength or constant k, the even and odd parts are reconstructed at nonoverlapping points in space (i.e., the zeros of the even part reconstruct at turning points of the odd part and vice versa). Therefore, it is possible to eliminate the conjugate image $b_{\text{real}}(-\mathbf{r})$ from the reconstruction of a single hologram data set by a suitable combination of $\tilde{b}_{\text{odd}}(\mathbf{r})$ and $\tilde{b}_{\text{even}}(\mathbf{r})$. For instance, $\tilde{b}_{\text{odd}}(\mathbf{r}) \sin(kr)$ and $\tilde{b}_{\text{even}}(\mathbf{r}) \cos(kr)$ can be summed with a moving box average of dimensions $\lambda/2$ to give $b(\mathbf{r})$. A consequence of this procedure is that the resolution of the reconstructed image is broadened by $\lambda/2$. Alternatively, the quality of the reconstructed image can be improved by combining holograms obtained at several different wavelengths.

For a single-point incoherent scatterer per unit cell, the above formulation will reconstruct the coherent scattering length with the incoherent scatterer located at the origin. For a uniformly random distribution of point incoherent scatterers, the reconstruction origin will be the "center of illumination," which by definition occupies exactly the same volume as the sample.

9.7 Inside Source Neutron Holography

The first inside source neutron holography experiments were carried out at the N5 triple-axis spectrometer (Fig. 9.3A) located at the NRU reactor at Chalk River Laboratories, Ontario. Those experiments used 1.3-Å neutrons with a $\Delta\lambda/\lambda \sim 1.5\%$ using the (113) reflection from a germanium (Ge) single-crystal monochromator. The sample-to-detector angular resolution was limited by distance collimation, defined by a combination of an aperture in neutron-absorbing cadmium masks and the size of the sample. Sample orientation (ϕ)

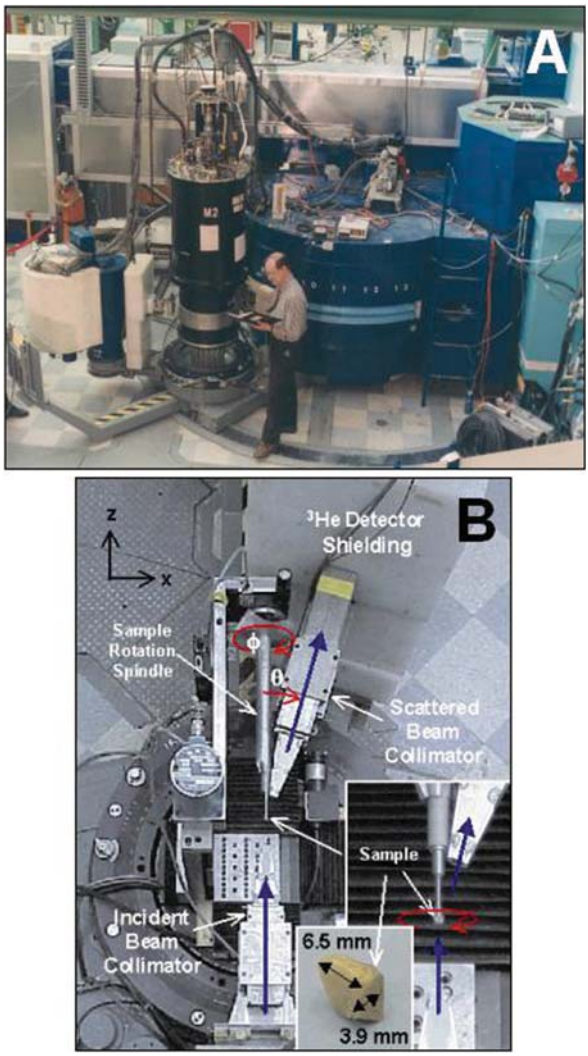

Fig. 9.3 (**A**) The N5 triple-axis spectrometer on which the first neutron holography experiments were carried out, located at the National Research Universal reactor, Chalk River Laboratories. (**B**) Plan view photograph and schematic of the neutron holography experimental setup at the N5 triple-axis spectrometer. The incident 1.3-Å neutron beam (originating from the bottom of the photograph) was parallel to the axis of rotation, ϕ. The angle between the detector and the ϕ axis is denoted by θ. In order to efficiently obtain the hemisphere of scattering, the crystal was rotated, in optimal ϕ steps of $2^\circ/\sin\theta$, from 0 to 2π for a given θ ($17^\circ \leq \theta \leq 83^\circ$). The lower value for θ (17°) was dictated as a result of the physical interference between the scattered beam collimator and the sample rotation spindle. The scattered neutrons were recorded using a ^{3}He detector. Figure adapted from Sur et al. [14]

and detector angle (θ) were manipulated in such a way that nearly a hemisphere of scattering was recorded (Fig. 9.3B). However, as a result of poor scattered intensity and a single-point detector, collecting good statistical quality data (total scattering and background) over 1.7π radians in scattering wavevector ($\mathbf{k}_{out}$) took ~10 days (Fig. 9.4A).

The structure of simpsonite contains two layers of oxygen atoms perpendicular to the *c* axis of the crystal lattice. The first layer, which is closest to the ^{1}H atom, has an oxygen atom located directly above (positive direction) the ^{1}H

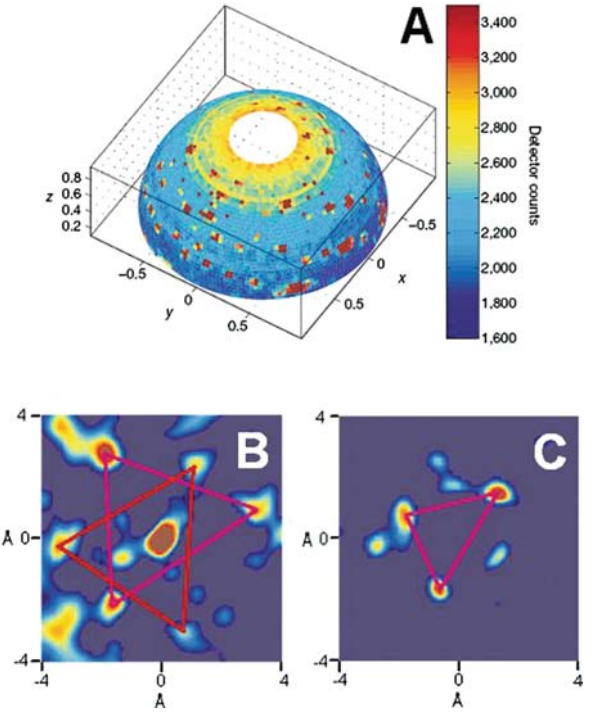

Fig. 9.4 (**A**) Raw hologram data containing 4,334 2° by 2° pixels plotted on a surface of constant scattered wave vector magnitude ($|\mathbf{k}_{out}| = 4.8$ Å^{-1}). Because of the experimental geometry, data collection was limited between 17 and 83° in θ, and about 13% of the pixels containing Bragg reflections were excluded from the reconstruction. The remaining data contained the hologram and θ-dependent background from the vanadium sample holder and aluminum wires (e.g., aluminum powder lines at $\theta = 32$, 37, 54, and 64°) used to secure the simpsonite crystal to the vanadium pedestal. (**B**) Reconstructed plane located approximately + 0.9 Å from the hydrogen atom at the origin showing the seven oxygen atoms. The plane is roughly coplanar to the basal plane of the crystal. The central spot is the oxygen atom located directly above the origin. The triangles are used to indicate the two triplets of oxygen atoms located slightly below this central oxygen atom. (**C**) Reconstructed plane located approximately –1.4 Å from the hydrogen atom at the origin showing the positions of the three oxygen atoms. The distortion of the triangles was attributed to limitations in the quality of the demonstration data. Figure adapted from Sur et al. [14]

atom along the direction of the *c* axis. This oxygen atom is surrounded by two triangular sublattices of oxygen atoms slightly below the position of the central oxygen atom. In the second layer, located below (negative direction) the ^{1}H atom, the oxygen atoms form triangular lattices about the perpendicular projection of the ^{1}H atom onto this layer.

Figure 9.4B shows a reconstructed plane, which is approximately coplanar to the basal plane, at a distance of $+0.9$ Å from the ^{1}H atom, which is at the origin of the reconstruction. There is a systematic distortion of the triangular lattices (Fig. 9.4B) owing to the just adequate counting statistics. Nevertheless, all of the expected oxygen atoms, six in the two triangles and the central atom, are present in the reconstruction. Figure 9.4C shows the next closest plane of oxygen atoms found at a distance of -1.4 Å from the origin. From the reconstruction, it is easily seen that these oxygen atoms form a triangle of nearest neighbors, albeit distorted.

9.8 Inside Detector Neutron Holography

The example discussed used a large incoherent neutron scatterer (i.e., hydrogen) to produce nearly *S* waves, "imaging" its surrounding atoms. By using the principle of optical reciprocity, the inside detector concept interchanges the positions of source and detector. In 2002, Cser et al. [16] demonstrated the feasibility of the inside detector technique to image lead (Pb) nuclei in a single crystal of Pb doped with the strong neutron absorber cadmium (Cd). In this case, Cd atoms act as point-like detectors, with a neutron wave reaching these detector nuclei either directly (reference beam) or after scattering from the Pb atoms in the crystal (object beam). The capture of neutrons by Cd results in the emission of γ radiation. The intensity of the γ radiation is directly proportional to the neutron intensity experienced by the detector nuclei. When recorded as a function of sample orientation with respect to the incident neutron beam, this fluctuating γ radiation intensity is effectively the hologram.

To demonstrate inside detector neutron holography, Cser et al. [16] used a 7-mm-diameter spherically shaped single crystal of $Pb_{0.9974}Cd_{0.0026}$ (the use of spherical samples greatly simplifies the data analysis). Cadmium atoms are strong neutron absorbers with a thermal absorption cross section over four orders of magnitude greater than that of Pb atoms [40]; this accounts for their ability to act as efficient detectors. The crystal structure of the $Pb_{0.9974}Cd_{0.0026}$ alloy is the same (face-centered cubic, fcc) as for pure lead [16], with the Cd atoms randomly distributed. As Cd was used in low concentrations, on average, every Cd atom was surrounded by 12 nearest-neighbor Pb atoms.

The (220) reflection from a Cu single crystal was used to select 0.8397-Å neutrons. Prompt γ radiation from the Cd nuclei was recorded using two scintillation counters shielded by $\sim$20 cm of lead. The sample was rotated

about its axis (ϕ) in 3° steps through ~350° and tilted (χ), also in 3° steps, through 120°. Figure 9.5A shows the reconstruction from the hologram of the 12 Pb atoms surrounding the detector Cd atom plotted in χ and ϕ coordinates, and Fig. 9.5B shows the Cd atom and its 12 neighboring Pb atoms plotted on the surface of a sphere of radius 3.49 Å. The x-axis is the direction of the incident neutron beam.

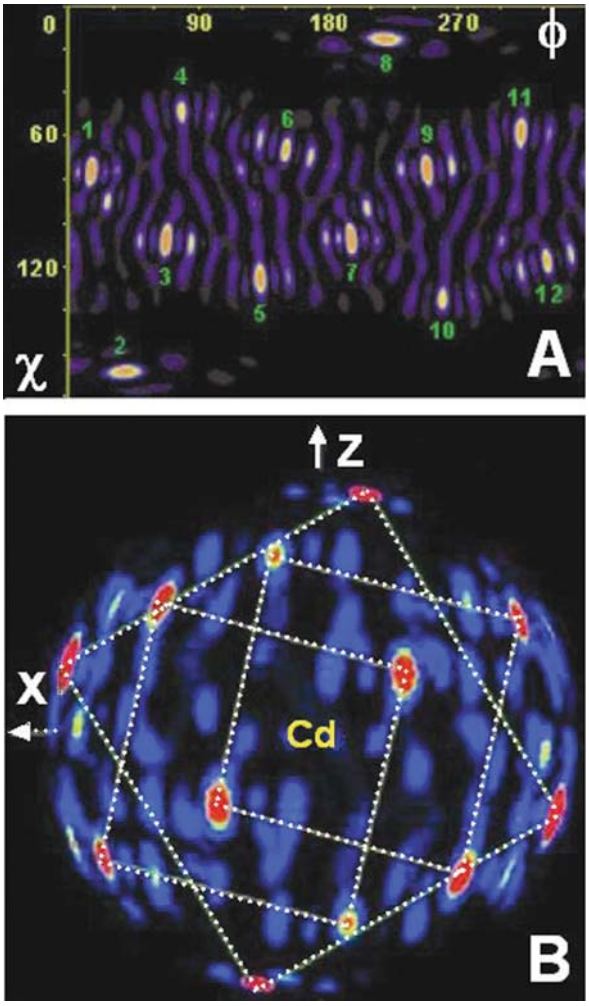

Fig. 9.5 (**A**) Reconstruction showing the positions of the 12 Pb atoms surrounding the detector Cd atom plotted in χ and ϕ coordinates. (**B**) The 12 Pb atoms surrounding the Cd detector atom plotted on the surface of a sphere of radius 3.49 Å. The x-axis denotes the direction of the incident neutron beam. Data were collected using the D9 diffractometer located at the Institute Laue-Langevin (Grenoble, France). Figure adapted from Cser et al. [16]

The most recent inside detector neutron holography study by Cser et al. [41] demonstrated for the first time the atomic positions with precision down to 1 picometer. To date, this is the only work based on a neutron holography experiment that contains information not previously made available by other experimental techniques.

9.9 Holographic Reconstruction from Multiple Incoherent Scatterers

The mathematical formulations for atomic structure holography have, until recently, been limited to samples with one S wave scatterer per unit cell. However, such samples are extremely rare. On the other hand, materials rich in hydrogen (e.g., biological or polymeric) are ubiquitous. Recently, Sur et al. [17] derived a kinematical formulation for the diffraction pattern of monochromatic plane waves scattering from a mixed coherent and incoherent scattering length distribution. From this second-order kinematical formulation, it became evident that samples with a uniformly random distribution of incoherent scatterers can be reconstructed to atomic resolution. Also, Sur et al. [17] provided a formulation for holographic reconstruction eliminating the so-called conjugate, or twin image problem, inherent in the holographic inversion of single-wavelength data.

9.10 Holography and Poorly Crystallized Proteins

Proteins are linear heteropolymers that play crucial roles in virtually all biological processes. The linear chain folds into an intricate 3D structure, which is determined by the sequence of amino acids, and is unique to each protein. It is this 3D structure that is the critical determinant of a protein's biological function. In principle, if one has knowledge of the amino acid sequence, it should be possible to predict the protein's 3D structure. However, a number of problems make this *ab initio* approach very difficult.

Traditionally, protein structures have been determined by X-ray diffraction (and to a much lesser extent by neutron diffraction) studies of crystallized samples and more recently, in the case of small (< 25 kDa) proteins in solution, by 2D and 3D nuclear magnetic resonance spectroscopy. In order to decipher the 3D structure using X-ray diffraction, well-ordered protein crystals must be available. However, the availability of quality crystals constitutes a major obstacle for traditional diffraction methods, particularly for those proteins integral to the cell's membrane. As a result, practically all of the approximately 34,000 known 3D protein structures are water soluble as opposed to membrane proteins. Fewer than 100 membrane proteins have been registered in the RCSB (Research Collaboratory for Structural Bioinformatics) protein data bank.

This is a critical shortfall since membrane-associated proteins are known to constitute approximately one-third of all known proteins [42], and approximately 40% of the human genome encodes for membrane proteins.

The first membrane-associated protein structure determined to near-atomic resolution (3 Å) was that of the photosynthetic reaction center of *Rhodopseudomonas viridis*, a purple sulfur photosynthetic bacterium whose 3D structure was solved by Deisenhofer et al. [43, 44]. In the case of the photoreaction center and other membrane-associated proteins, [45–47] detergents were essential to producing high-quality crystals suitable for Bragg and Laue diffraction studies. At present there does not appear to be a systematic method for obtaining high-quality crystals for the majority of membrane proteins. However, low-quality membrane protein crystals, which do not diffract to high resolution, may be more readily obtainable using the present crystal growing techniques. The concept in holography is to reconstruct the local atomic structure in the vicinity of the source or the detector atoms. Thus long-range translational order (i.e., periodicity) of the protein unit cell structure is not required for a solvable hologram. The only requirement is that the unit cells be oriented in the same direction (within an acceptable mosaic spread, consistent with the unit cell dimensions). Thus poor crystals or quasicrystals are especially useful candidates for the determination of atomic-resolution 3D structure via holography.

Depending on the protein's chemistry, thermal neutron and X-ray holography techniques may be used to resolve, to atomic resolution, the 3D structure of proteins forming either poor crystals or quasicrystals. One strategy may be to start with a low-resolution ($\sim$ 6 Å data) 3D X-ray structure that can be refined to atomic resolution using the appropriate X-ray or neutron hologram of the protein. Assuming that the quasi-protein crystal contains only positional and not orientational disorder, this strategy, if successful, will enable atomic-resolution studies of an entire class of macromolecules with structures that are inaccessible presently and for the foreseeable future. However, there are potential difficulties.

Until now the mathematical formulations for atomic structure holography have been limited to samples with one source atom per unit cell (not common). As mentioned, Sur et al. [17] have mathematically formulated the reconstruction of samples with multiple source atoms per unit cell. In practice, for thermal neutron holography, this condition can be realized when the samples used have a uniformly random distribution of hydrogen atoms, an approach very much analogous to that of the commonly used diffuser in optical holography. However, the experimental feasibility of this proposed technique has yet to be demonstrated. On the other hand, if this approach proves to be feasible, holographic techniques will drive a worldwide expansion of knowledge about the 3D structure of membrane-associated proteins and other macromolecules, leading to better insights into biological processes and improved designs of existing drugs.

9.11 The Future

The technique of atomic-resolution holography is not yet established for routinely determining atomic structure. It is, however, a promising and technically feasible method for solving problems that cannot be resolved with traditional diffraction methodologies. Presently, there has yet to be an atomic-resolution holography study using a sample that could not be successfully studied using traditional crystallography (i.e., a poor crystal or quasicrystal).

A recent technological advance challenging the holographic techniques described is the development of hard X-ray free electron lasers (XFELs), making coherent X-ray diffraction imaging a possibility. The first XFEL, the Linac Coherent Light Source at the Stanford Linear Accelerator Center, is slated to begin experiments in 2009. The European XFEL Facility [48] (Germany) will follow in 2013. Unlike third-generation synchrotron sources, which use lenses to produce coherent X rays, the inherently coherent X-ray beams produced by XFELs have the potential to image materials with 10 times better spatial resolution. XFEL sources thus offer the possibility to resolve structural details of materials to atomic resolution with high-brilliance femtosecond coherent X-ray pulses. In a study headed by scientists from Lawrence Livermore National Laboratory, a soft XFEL ($\lambda = 320$ Å) was used to demonstrate that a coherent diffraction pattern from a nonperiodic object could be obtained prior to destroying the sample at 60,000 K [49].

9.12 Concluding Remarks

This brief review has presented the current state of neutron holography. Neutron holography is a nondestructive, *in situ* technique capable of atomic-resolution measurements of biologically relevant materials and appears to be an excellent option for the solution of poorly crystallized or quasicrystal proteins. However, an experimental demonstration of "diffuse source" atomic-resolution holography, utilizing incoherent scattering from the large numbers of hydrogen atoms in biological materials, is key to future developments. Future neutron holography experiments will benefit greatly from spallation source instruments capable of acquiring neutron scattering data with simultaneous large solid angle coverage and at multiple wavelengths, capabilities that will become available at the Spallation Neutron Source.

References

1. W.L. Bragg, The X-ray microscope. *Nature* **149,** 470 (1942).
2. D. Gabor, A new microscopic principle. *Nature* **161,** 777–778 (1948).
3. G.R. Harp, D.K. Saldin, and B.P. Tonner, Atomic resolution holography in solids with localized sources. *Phys. Rev. Lett.* **65,** 1012–1015 (1990).

4. M. Zharnikov, M. Weinelt, P. Zebish, S M. tichler, and H. -P. Steinrück, First experimental determination of an adsorption site using multiple wave number photoelectron diffraction patterns. *Phys. Rev. Lett*. **73,** 3548–3551 (1994).
5. M.T. Sieger, J.M. Roesler, D. -S. Lin, T. Miller, and T. -C. Chiang, Holography of Ge(111)-c(2×8) by surface core-level photoemission. *Phys. Rev. Lett*. **73,** 3117–3120 (1994).
6. A. Orchowski, W. D. Rau, and H. Lichte, Electron holography surmounts resolution limit of electron microscopy. *Phys. Rev. Lett*. **74,** 399–402 (1995).
7. T. Matsushita, F.Z. Guo, F. Matsui., Y. Kato., and H. Daimon, Three-dimensional atomic-arrangement reconstruction from an Auger-electron hologram. *Phys. Rev. B* **75,** 085419(1)–085419(5) (2007).
8. M. Tegze and G. Faigel, Atomic resolution X-ray holography. *Europhys. Lett*. **16,** 41–46 (1991).
9. T. Gog., P.M. Len, G. Materlik., D. Bahr., C.S. Fadley, C. Sanchez-Hanke, Multiple-energy holography: Atomic images of hematite (Fe_2O_3). *Phys. Rev. Lett*. **76,** 3132–3135 (1996).
10. M. Tegze and G. Faigel. X-ray holography with atomic resolution. *Nature* **380,** 49–51 (1996).
11. M. Tegze, G. Faigel, S. Marchesini, M. Belakhovski, and A.I. Chumakov, Three dimensional imaging of atoms with isotropic 0.5 Å resolution. *Phys. Rev. Lett*. **82,** 4847–4850 (1999).
12. S. Eisebitt, J. Lüning, W.F. Schlotter, M. Lörgen, O. Hellwig, W. Eberhardt, and J. Stöhr, Lensless imaging of magnetic nanostructures by X-ray spectro-holography. *Nature* **432,** 885–888 (2004).
13. H.N. Chapman, et al. Femtosecond time-delay X-ray holography. *Nature* **448,** 676–670 (2007).
14. B. Sur, R.B. Rogge, R.P. Hammond, V.N.P. Anghel, and J. Katsaras, Atomic structure holography using thermal neutrons. *Nature* **414,** 525–527 (2001).
15. B. Sur, R.B. Rogge, R.P. Hammond, V.N.P. Anghel, and J. Katsaras Observation of Kossel and Kikuchi lines in thermal neutron incoherent scattering. *Phys. Rev. Lett*. **88,** 065505(1)–065505(4) (2002).
16. L. Cser, Gy. Török, G. Krexner, I. Sharkov, and B. Faragó, Holographic imaging of atoms using thermal neutrons. *Phys. Rev. Lett*. **89,** 175504(1)–175504(4) (2002).
17. B. Sur, V.N.P. Anghel, R.B. Rogge, and J. Katsaras, Diffraction pattern from thermal neutron incoherent elastic scattering and the holographic reconstruction of the coherent scattering length distribution. *Phys. Rev. B* **71,** 014105(1)–014105(12) (2005).
18. P.G. Tanner, and T.E. Allibone, The patent literature of Nobel laureate Dennis Gabor (1900 – 1979). *Notes Rec. R. Soc. Lond*. **51,** 105–120 (1979).
19. A.L. Schawlow, and Townes C.H. Infrared and optical masers. *Phys. Rev*. **112,** 1940–1949 (1958).
20. A.L. Schawlow, and Townes C.H. U.S. patent no. 2,929,222 (March 22, 1960).
21. A. Einstein, *Zur quantentheorie der strahlung. Physik. Zeitschr*. **18,** 121–128 (1917).
22. Y.N. Denisyuk, On the reflection of optical properties of an object wave field scattered by it. *Doklady Akademii Nauk SSSR* **144,** 1275–1278 (1962).
23. E.N. Leith, and J. Upatnieks, Reconstructed wavefronts and communication theory. *J. Opt. Soc. Am*. **52,** 1123–1130 (1962).
24. A. Szöke, X-ray and electron holography using a local reference beam, in Short Wavelength Coherent Radiation: Generation and Applications, eds. D.J. Attwood, and J. Boker AIP Conf. Proc. No. 147, pp. 361–467 (American Institute of Physics, 1986).
25. S. Kikuchi, Diffraction of cathode rays by mica. *Jpn. J. Phys*. **5**, 83–96 (1928).
26. W. Kossel, V. Loeck, and H. Voges, Die richtungsverteilung der in einem kristall entstandenen charakteristichen Röntgenstrahlung. *Z. Phys*. **94,** 139–142 (1935).
27. T. Gog, D. Bahr, and G. Materlik, Kossel diffraction in perfect crystals: X-ray standing waves in reverse. *Phys. Rev. B* **51,** 6761–6764 (1995).

28. G. Faigel, and M. Tegze, X-ray holography. *Rep. Prog. Phys.* **62,** 355–393 (1999).
29. J. Chadwick, Possible existence of a neutron. *Nature* **129,** 312 (1932).
30. J. Chadwick, The existence of a neutron. *Proc. Roy. Soc. (London)* **A136,** 692–708 (1932).
31. E. Rutherford, Nuclear constitution of atoms. *Proc. Roy. Soc.* **A97,** 374–400 (1920).
32. W. Mampe, P. Ageron, C. Bates, J.M. Pendelbury, and A. Steyerl, Neutron lifetime measured with stored ultracold neutrons. *Phys. Rev. Lett.* **63,** 593–596 (1989).
33. B. Jacrot, The study of biological structures by neutron scattering from solution. Rep (sp. nov.) from Tabba Tabba, western Australia. *J. R. Soc. W. Aust. Prog. Phys.* **39**, 911–953 (1976).
34. L. Cser, G. Krexner, and Gy. Török, Atomic resolution neutron holography. *Europhys. Lett.* **54**, 747–752 (2001).
35. H. Bowley, Simpsonite (sp. nov) from Tabba Tabba, western Australia. *J. R. Soc. W. Aust.* **25,** 89–92 (1939).
36. L.E.R. Taylor, X-ray studies of Simpsonite. *J. R. Soc. W. Aust.* **25,** 93–97 (1939).
37. T.S. Ecrit, Ćerný, P., and F.C. Hawthorne, The crystal chemistry of Simpsonite. *Can. Mineral.* **30,** 663–671 (1992).
38. G.L. Clark, and W. Duane, A new method of using x-rays in crystal analysis. *Proc. Natl. Acad. Sci. U.S.A.* **8**, 90–96 (1922).
39. M. v. Laue, Die fluoreszensröntgenstrahlung von einkristallen. *Ann. Physik* **23,** 705–746 (1935).
40. V.F. Sears Neutron scattering lengths and cross sections. *Neutron News* **3**, 26–37 (1992).
41. L. Cser, G. Krexner, Markó, M., I. Sharkov, and Gy. Török, Direct observatotion of local distortion of a crystal lattice at picometer accuracy using atomic resolution neutron holography. *Phys. Rev. Lett.* **97,** 255501(1)–255501(4) (2006).
42. A. Goffeau, Life with 482 genes. *Science* **270,** 445–446 (1995).
43. J. Deisenhofer, O. Epp, K. Miki, R. Huber, and H. Michel, X-ray structure analysis of a membrane protein complex: electron density map at 3 Å resolution and a model of the chromophores of the photosynthetic reaction center from *Rhodopseudomonas viridis*. *J. Mol. Biol.* **180,** 385–398 (1984).
44. J. Deisenhofer, O. Epp, K. Miki, R. Huber and H. Michel, Structure of the protein subunits in the photosynthetic reaction center of *Rhodopseudomonas viridis* at 3 Å resolution. *Nature* **318,** 618–624 (1985).
45. M. Garavito and J.P. Rosenbusch, Isolation and crystallization of bacterial porin. *Meth. Enzymol.* **125,** 309–328 (1986).
46. S.W. Cowan, et al., The structure of OmpF porin in a tetragonal crystal form. *Structure* **3,** 1041–1050 (1995).
47. R. Dutzler, et al., Crystal structure and functional characterization of OmpK36, the osmoporin of *Klebsiella pneumoniae*. *Structure* **7,** 425–434 (1999).
48. I.A. Vartanyants, I.K. Robinson, I. McNulty, C. David, P. Wochner, and Th. Tschentscher, Coherent X-ray scattering and lensless imaging at the European XFEL Facility. *J. Synch. Rad.* **14,** 453–470 (2007).
49. H.N. Chapman, et al., Femtosecond diffractive imaging with a soft-X-ray free-electron laser. *Nat. Phys.* **2**, 839–843 (2006).